Acta Materialia 233 (2022) 117979

Contents lists available at ScienceDirect

Acta Materialia

journal homepage: www.elsevier.com/locate/actamat

Unveiling the Re effect on long-term coarsening behaviors of γ' precipitates in Ni-based single crystal superalloys

Fan Lu[a], Stoichko Antonov[b], Song Lu[a], Jiachen Zhang[c], Longfei Li[a,*], Dong Wang[d], Jian Zhang[d], Qiang Feng[a,*]

[a] Beijing Advanced Innovation Center for Materials Genome Engineering, State Key Laboratory for Advanced Metals and Materials, University of Science and Technology Beijing, Beijing, 100083, China
[b] Department of Microstructure Physics and Alloy Design, Max-Planck-Institut für Eisenforschung GmbH, 40237 Düsseldorf, Germany
[c] State Key Laboratory of Solidification Processing, Northwestern Polytechnical University, Xi'an 710072, China
[d] Superalloys Division, Institute of Metal Research, Chinese Academy of Sciences, Shenyang 110016, China

ARTICLE INFO

Article history:
Received 25 August 2021
Revised 24 April 2022
Accepted 24 April 2022
Available online 26 April 2022

Keywords:
Nickel-based single crystal superalloy
Rhenium-effect
Long-term thermal exposure
Atom-probe tomography
Coarsening kinetics

ABSTRACT

In response to the increased demand for very long-term service reliability of industrial gas turbine (IGT) blades, the microstructural stability of two single crystal (SX) superalloys with different Re addition (0Re and 2Re in wt.%, named as alloy 0Re5Ta and 2Re5Ta) were investigated during long-term thermal exposure (>5000 h) at 900 °C, with the help of atom probe tomography (APT) and high-temperature X-ray diffraction (XRD) analysis. During long-term thermal exposure, the γ' precipitates coarsened gradually in both alloys. At the same time, the γ' precipitates became more cuboidal for alloy 0Re5Ta and nearly spherical for alloy 2Re5Ta due to the increased positive lattice misfit for alloy 0Re5Ta and the decreased negative lattice misfit for alloy 2Re5Ta. Such lattice misfit evolution was mainly attributed to the inversion of the W partitioning from γ matrix to γ' precipitates over time. The addition of Re can effectively decrease the coarsening rate during thermal exposure. Further investigations on the coarsening kinetics confirmed the Re effect on reducing the interfacial energy and enhancing the rate-limiting effect of Cr. Additional particle size distributions (PSDs) showed a gradual transition from the initial matrix-diffusion coarsening-controlled mechanism to the interface-diffusion coarsening-controlled mechanism at prolonged time, wherein Re triggered the interface-diffusion mechanism earlier by leading to sharper interfaces. Although Re increases the magnitude of the lattice misfit in the initial microstructure, it can significantly enhance the microstructural stability of SX superalloys for IGT application.

© 2022 Acta Materialia Inc. Published by Elsevier Ltd. All rights reserved.

1. Introduction

Commercial Ni-based single crystal (SX) superalloys are considered state-of-the-art alloys and are highly optimized to meet the demands of the hot-sections of advanced aircraft engines [1]. The good comprehensive high-temperature properties of Ni-based SX superalloys are achieved by tailoring the distribution and composition of the coherent γ' precipitates that are dispersed in a solid-solution strengthened γ matrix, where both phases are directly depended on the particular alloy's composition and heat-treatment [2,3]. However, these highly-optimized superalloys are not suitable for manufacturing industrial gas turbine (IGT) blades, which operate in harsh service environments and at relatively low and steady temperatures, but more importantly, for much longer lifetimes compared to aero-engine blades [4]. The distinctive service conditions of IGT blades create great necessity for the development of new materials to sustain the stable operation of IGT blades, for which a better understanding of the time-dependent processes (at much longer time-scales than aero-engines) is crucial.

Microstructural evolution during thermal exposure is a major concern for the structural reliability of the materials, especially for prolonged service [5,6]. Thermal exposure of superalloys can lead to microstructural instabilities such as the morphological evolution of γ' precipitates (the morphology, size and distribution) [7,8]. The morphological evolution of γ' precipitates is itself also influenced by the γ/γ' lattice misfit, which is attributed to the elemental partitioning behavior between γ matrix and γ' precipitate. Typical Ni-based SX superalloys possess negative lattice misfit, yielding considerable creep resistance at high temperatures [9,10]. The lattice misfit, associated with the elemental partitioning behavior, has

* Corresponding authors.
E-mail addresses: lilf@skl.ustb.edu.cn (L. Li), qfeng@skl.ustb.edu.cn (Q. Feng).

https://doi.org/10.1016/j.actamat.2022.117979
1359-6454/© 2022 Acta Materialia Inc. Published by Elsevier Ltd. All rights reserved.

been shown to substantially shift after long-term creep in our previous research [11].

As the stability of the ordered precipitates can pose adverse effects to the mechanical properties of superalloys, the precipitate coarsening and the γ/γ' coherency stress evolution during aging have been thoroughly studied [8,12]. A classical theory to quantitatively describe precipitate coarsening kinetics, also termed Ostwald ripening, was first postulated by Lifshitz and Slyozof [13] and then by Wagner (known as LSW theory) [14]. However, the LSW theory, which is based on binary systems, assumes a dilute system, i.e., with low precipitate volume fraction, in which particle-particle interactions are not considered. To address issues with this assumption, more realistic models were subsequently developed to modify the LSW theory by taking into account the effect of particle volume fraction, such as the Modified LSW (MLSW, 1972) [15], Davies-Nash-Stevens (LSEM, 1980) [16], Brailsford-Wynblatt (BW, 1979) [17], etc. In multi-component alloys, the interaction and diffusion of different elements lead to a further consideration of the interfacial mass balance equation, other than the local equilibrium which is not sufficient to determine the interfacial composition present by Gibbs-Thompson equation. Thus, Kuehmann and Voorhees (K-V) [18] developed a model to describe Ostwald ripening in a ternary alloying system, without considering the off-diagonal diffusion coefficient. More recently, Philippe and Voorhees (P-V) [19] proposed a generalized model to describe coarsening in multi-component alloys, taking advantage of the latest thermodynamic and atomic mobility databases.

Ardell and Ozolins developed a different model – the so-called trans-interface diffusion-controlled (TIDC) model – proposing that the diffusion through the interface, rather than matrix diffusion, controls the coarsening process [20–22]. The TIDC model deals with the effect of the interfacial width and particle distribution and excludes the effect of precipitate volume fraction. This model has been successfully applied for the γ' coarsening of the commercial multi-component superalloy René 88DT [7]. Furthermore, Sun [23] proposed that a competition between matrix diffusion and interface reaction does not only exist in different coarsening system, but within different stages in a single coarsening process. Zhang et al. [24] further demonstrated an underlying mechanism change from matrix-diffusion controlled coarsening and interface-diffusion controlled coarsening during long-term isothermal aging by thorough analysis of the particle size distributions (PSDs). As can be seen from the above, precipitate coarsening is a very complex yet important aspect of alloy design, with different competing theories that have been applied (with various levels of success) to model and commercial alloys. As an important alloying addition in superalloys, Re has been shown to yield considerable microstructural stabilities and high-temperature creep properties due to its low diffusivity and high solid solution strength [2]. Recent studies have shown that Re is also helpful for the oxidation and corrosion resistance of superalloys [25,26]. Therefore, development of novel Ni-based SX superalloys with Re additions may help attain superior properties for IGT blades. However, little is known about the effect of Re on the change in coarsening rate controlling mechanism and a possible transition from matrix-diffusion controlled coarsening to interface-diffusion controlled coarsening during long-term thermal exposure. To address this, atom probe tomography (APT) can be utilized to obtain information of the partitioning behaviors and interfacial characteristics between the γ and γ' phases at the near-atomic scale [27–30].

In this work, we used APT and high-temperature X-ray diffraction (XRD) to examine the microstructural evolution during thermal exposure of a Re-free and a Re-containing superalloy and relate it to the evolution of the elemental partitioning behavior and the lattice misfit. In order to deduce the effect of Re, the interfacial energy was estimated and the rate-limiting element was determined by evaluating the coarsening rate in different coarsening models. By comparing the PSDs evolution within the two extreme cases, referring to the matrix-diffusion controlled mechanism and interface-diffusion controlled mechanism, the dominant coarsening-controlled mechanisms were clarified. This work reveals important implications for optimizing the long-term microstructural stability of Ni-based SX superalloys designed for the IGT blades.

Table 1
Nominal compositions of the experimental alloys (in wt.%).

Alloy	Re	Co	Cr	Mo	W	Al	Ta	Ti	Ni
0Re5Ta	0	10	10	0.5	4.5	4	5	3	Bal.
2Re5Ta	2	10	10	0.5	4.5	4	5	3	Bal.

2. Experimental

The nominal compositions of the experimental alloys are given in Table 1, with the only distinction of 2 wt.% Re addition to alloy 2Re5Ta. The single crystal bars were directionally solidified along the [001] orientation and subjected to a suitable solution and aging treatment (1230 °C /2 h+1255 °C /2 h; 1130 °C /4 h+870 °C /20 h for alloy 0Re5Ta; 1240 °C /2 h+1265 °C /2 h; 1130 °C /4 h+870 °C /20 h for alloy 2Re5Ta). The alloys directly after this heat treatment are referred to as "Initial" state throughout this research. Long-term thermal exposure samples were obtained by hanging Ø15 mm × 20 mm bulk samples inside the creep-frame furnace during the creep testing of the samples presented in our previous publication [11], and cooled to room temperature in air once creep rupture occurred. This allows for a direct comparison of samples subjected to the same temperature, time and environment, but with different loading conditions. The thermal exposure at 900 °C corresponding to the rupture time was 2398 h for alloy 0Re5Ta, and 5589 h for alloy 2Re5Ta. In order to analyze the coarsening kinetics, samples of both alloys were also thermally exposed at 900 °C for shorter durations by interrupted experiments (425 h and 1800 h, corresponding to the creep rate minimum of the alloy 0Re5Ta and alloy 2Re5Ta, respectively, as indicated in Ref. [11]).

Standard metallographic specimens were prepared for microstructural investigation and etched in a solution of 1% HF-33% CH_3COOH-33% HNO_3-33% H_2O (volume fraction) to selectively dissolve the γ' phases. Microstructural observations were performed in a ZEISS SUPRA 55 field-emission scanning electron microscope (SEM) in secondary electron (SE) mode. The Image J and Image-Pro Plus softwares were used to quantify the microstructural evolution, including the volume fraction, size and shape parameter of γ' precipitates. The shape parameter, η, was used to determine the γ' morphology, and a schematic diagram of the method is shown in Fig. 1 [31]. In this method, the marked length parameter "A" is the edge length of a square and "B" is the actual length of the γ' precipitate. The Kappa plugin (GitHub - fiji/Kappa: A Fiji plugin for Curvature Analysis) in Image J software was used to distinguish the transition point from the curvature of zero to that of non-zero, allowing for accurate measurement of A and B for each precipitate. The shape parameter, η, was defined as $\eta = A/B$, wherein a value of $\eta = 0$ corresponds to an absolutely spherical shape and $\eta = 1$ refers to an absolutely cuboidal shape.

The γ and γ' lattice parameters at 900 °C were measured using an advanced Bruker D8 discover high-resolution X-ray diffractometer (XRD) operating at 900 °C. All samples were heated from room temperature (RT) to 900 °C at a rate of 50 °C/min in a vacuum chamber at $< 10^{-4}$ mbar. An extra 10 min soaking time was needed to ensure temperature homogeneity throughout the test-

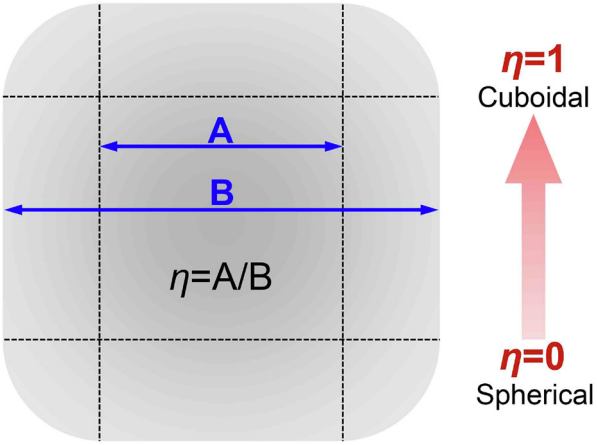

Fig. 1. Shape parameter (η) to quantitatively assess the γ' precipitate morphology (Adapted from Ref. [31])

ing samples. The (001) superlattice peaks were measured for every sample to accurately determine the lattice parameter of γ' phase, and two-phase overlapping (004) reflections were recorded and deconvoluted using Jandel Scientific PeakFit commercial software.

The recorded profiles were properly fitted using three Pseudo-Voigt functions, corresponding to one sub-peak for γ' precipitates and two sub-peaks for γ matrix (corresponding to the vertical and horizontal γ channels). This is required for such highly asymmetric peak profiles, which arises as a consequence of the tetragonal lattice distortion of the thin γ matrix channels. This distortion is caused by the biaxial internal stresses within the channels, that are induced by the coherency stresses at the γ/γ' interface [32]. The lattice parameter of the γ matrix can be calculated by the following Eq. (1) described in Ref. [33]:

$$a_\gamma = \frac{(S_{11}+S_{12})a_{\gamma,h} - 2S_{12}a_{\gamma,v}}{S_{11}-S_{12}} \quad (1)$$

where S_{11} and S_{12} are the elastic compliance tensors of pure γ-Ni. The typical values are $S_{11} = 0.799 \times 10^{-5}$/MPa and $S_{12} = -0.321 \times 10^{-5}$/MPa, which are taken from Ref. [1]. The $a_{\gamma,h}$ and $a_{\gamma,v}$ are the lattice parameters coming from the subpeaks of the horizontal and vertical γ channels. Consequently, the overall γ/γ' lattice misfit (δ) can be calculated as follows:

$$\delta = \frac{2\left(a_{\gamma'} - a_\gamma\right)}{a_{\gamma'} + a_\gamma} \quad (2)$$

where $a_{\gamma'}$ and a_γ are the lattice parameters for γ and γ' phases, respectively.

To accurately determine the elemental partitioning across the γ and γ' interface, APT samples were prepared from the dendrite cores of all samples via a standard lift-out procedure by focused ion beam (FIB) similar to ref. [34] on a FEI Helios nanolab 600i. APT measurements were carried out on a CAMECA LEAP 5000 XR instrument operating in laser pulse mode (wavelength of 355 nm) with a pulse energy of 25 pJ per pulse, a pulse rate of 125 kHz and an evaporation rate of 0.5% at a base temperature of 35 K. All of the APT data was analyzed by IVAS 3.8.8 software from CAMECA.

To evaluate the strength of the γ' phase, nanoindentation tests were carried out using Hysitron Ti980 nano mechanical tester with a Berkovich diamond indenter under 500 μN load at room temperature (Ti980 Hysitron). Additionally, the strength of the whole alloy was gauged by random microhardness tests performed with 1000 μN load to simultaneously cover the γ and γ' phase by the bigger indentation.

3. Results

3.1. Morphological evolution of γ' precipitates during thermal exposure

Representative γ/γ' micrographs of the two experimental alloys after full heat-treatment and after thermal exposure at 900 °C for different durations are presented in Fig. 2. For a better comparison, the observations are all taken from the dendrite cores, where the precipitate morphologies are more regular. The temporal changes of microstructural parameters, including γ' volume fraction, γ' size and shape parameter, were quantitatively measured and listed in Table 2. In the initial state, cuboidal γ' precipitates comprised 55.7% and 57.3% in volume for alloys 0Re5Ta and 2Re5Ta, respectively, and were dispersed homogeneously in the matrix, forming narrow γ channels throughout the samples. The addition of Re refined the size of γ' precipitates and increased the shape parameter in the initial state. When subjected to thermal exposure at 900 °C, TCP phases did not precipitate and normal coarsening behavior occurred, i.e. no precipitate splitting [35,36], accompanied by a slight dissolution of γ' phase to a volume fraction of ~52% for both alloys. For alloy 0Re5Ta, γ' precipitates had an average radius of 210 nm in the initial state and gradually grew to ~448 nm during thermal exposure up to 2398 h. Concurrently, the value of η increased from 0.21 to 0.32, thus the γ' morphology with sharper corners occurred (more cuboidal). Meanwhile, for alloy 2Re5Ta, the γ' radius coarsened from ~135 nm in the initial state to ~458 nm during the thermal exposure time of 5589 h. Although the precipitates in the initial state were more cuboidal in alloy 2Re5Ta compared to alloy 0Re5Ta, they transitioned to irregular spherical morphology with apparent interconnection, and the value of η decreased from 0.37 to 0.15. Here, the standard deviations of the shape parameters were below 0.04 and 0.06 for alloy 0Re5Ta and alloy 2Re5Ta, respectively, which is not included in Table 2. Clearly, the addition of Re changed the morphological evolution tendency.

3.2. Calculated coarsening rate within different temporal exponent

During thermal exposure, the microstructural evolution of the precipitates approximately follows an Ostwald ripening process, which can be described by a power-law equation, as follows [37]:

$$\langle R(t)\rangle^n - \langle R(t_0)\rangle^n = k(t - t_0) \quad (3)$$

where t_0 is the time for the onset of quasi-stationary coarsening, $R(t)$ is the average precipitate radius at the thermal exposure time t, $R(t_0)$ is the average precipitate radius at $t = t_0$, k is the coarsening rate constant and n is the temporal exponent. Upon fitting the coarsening datasets by linear regressions with different values of the temporal exponent n, the coarsening rate can be measured and compared with classical coarsening theories. When $n = 3$, the coarsening rate can be obtained by a linear fitting of $\langle R(t)\rangle^3$ versus t, which is widely known as the classical LSW theory, related to the matrix-diffusion controlled coarsening. When $n = 2$, the coarsening rate can be obtained by a linear fitting within $\langle R(t)\rangle^2$ versus t, the so-called the TIDC theory, related to the interface-diffusion controlled coarsening. Lastly, in accord with the more reasonable P-V model which is valid for the multi-component alloys, the non-linear regression with an unknown and non-integer temporal exponent n provides a more accurate mathematical treatment to the practical coarsening datasets. Multivariate non-linear regression analysis is then applied to determine the unknown parameters t_0, $R(t_0)$, k and n in Eq. (3).

In order to measure and compare the coarsening rate within a certain temporal exponent, following the standard Ostwald ripen-

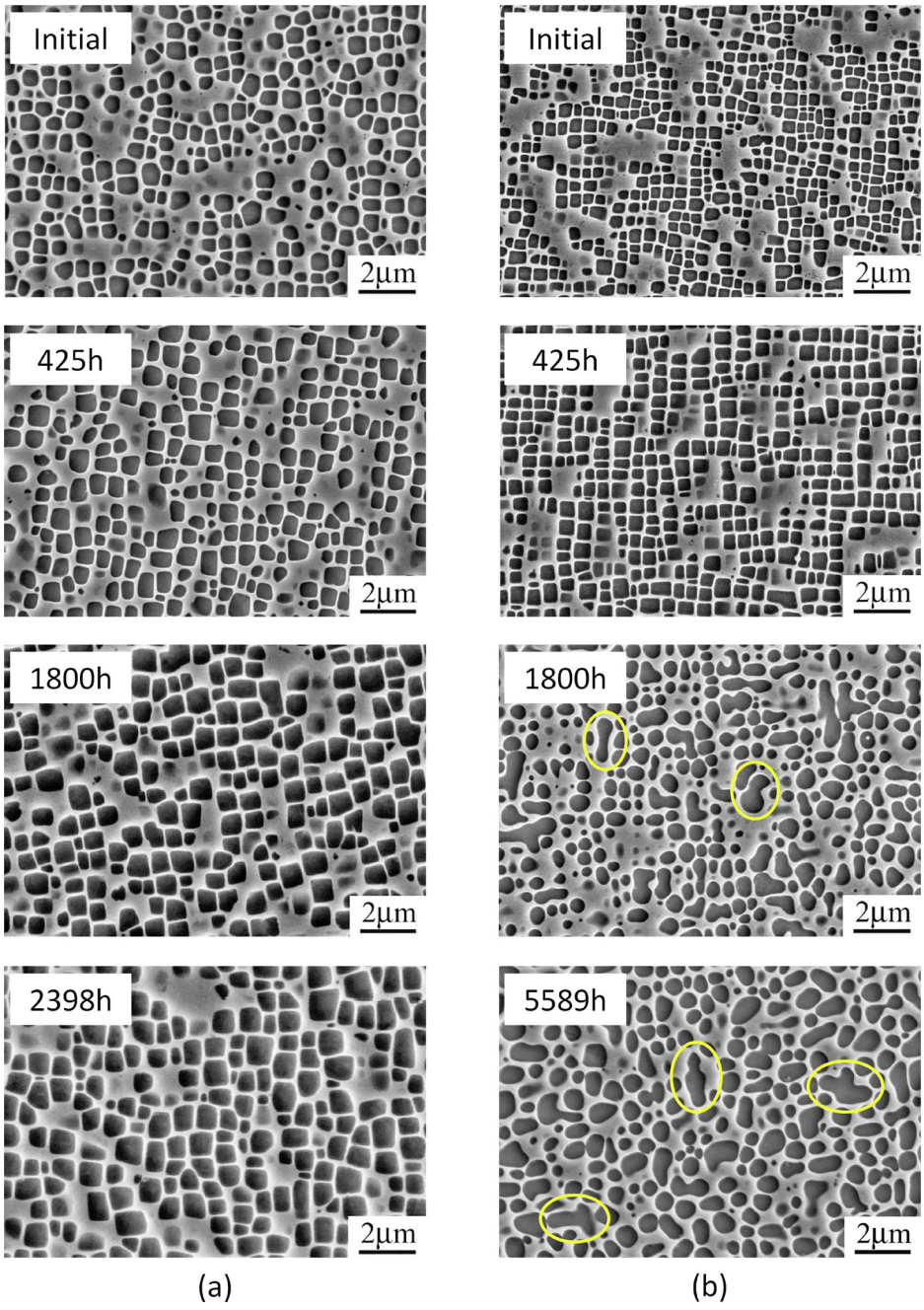

Fig. 2. γ/γ' microstructures at the initial state and after thermal exposure for different durations at 900 °C of (a) alloy 0Re5Ta and (b) alloy 2Re5Ta.

Table 2
Temporal changes of microstructural parameters for alloys 0Re5Ta and 2Re5Ta during thermal exposure at 900 °C.

Alloy	Time [h]	γ' volume fraction [%]	γ' radius [nm]	γ' shape parameter η
0Re5Ta	0	55.7±1.0	210±59	0.21
	425	53.6±1.6	288±74	0.24
	1800	52.8±2.2	411±78	0.29
	2398	51.5±1.2	448±126	0.32
2Re5Ta	0	57.3±1.3	135±39	0.37
	425	56.1±2.1	201±63	0.35
	1800	53.2±2.8	315±151	0.20
	5589	51.9±2.7	458±137	0.15

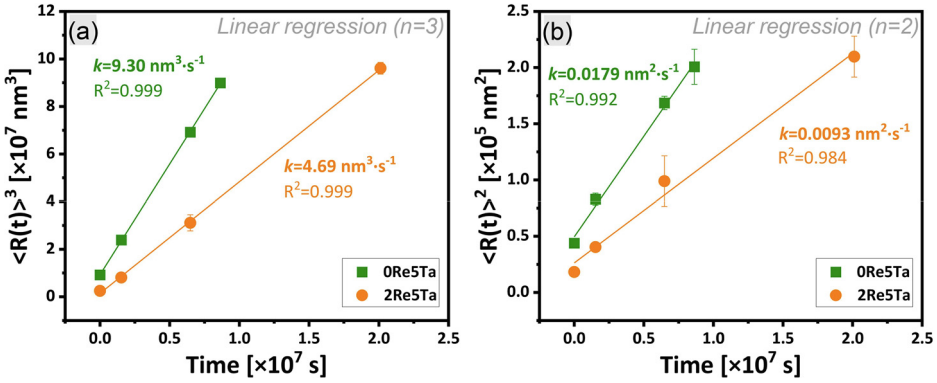

Fig. 3. Plots of the average precipitate radius, $R(t)$ (raised to the nth power) versus thermal exposure time. Linear regressions are employed for different temporal exponent (a) $n=3$ and (b) $n=2$.

Table 3
Coarsening parameters, t_0, $R(t_0)$ and n, in Eq. (3), together with the coarsening rate constants k determined by non-linear regression analysis of the experimental average precipitates sizes.

Alloy	Non-linear regression				Linear regression	
	t_0 (h)	$R(t_0)$(nm)	n	k (nm^n·s^{-1})	$k_{(n=3)}$ (nm^3·s^{-1})	$k_{(n=2)}$ (nm^2·s^{-1})
0Re5Ta	4.7±0.3	210.6±1.1	2.82±0.14	3.14±0.03	9.30	0.0179
2Re5Ta	8.3±0.7	136.3±1.3	2.74±0.17	0.96±0.05	4.69	0.0093

*Note: the coarsening rate constants in the non-linear regressions should have inaccurate dimensions since the non-integer n. The coarsening rate constants determined by linear regressions are also listed here.

ing theory, the classical LSW theory and further TIDC theory represent distinct coarsening control mechanisms, for which the cube rate law and square rate law, respectively, should be used to fit the precipitate sizes as a function of time. A linear regression of the cube and square of the average precipitate radius in the two experimental alloys versus time plots are shown in Fig. 3. It should be mentioned that all the precipitate sizes of each alloy are included in the analysis since the γ' volume fractions possess very limited deteriorations from the initial state to thousands of hours of thermal exposure time for both alloys. The coarsening rates are the slopes of the fitting lines and are also shown in Fig. 3, along with the correlation coefficient, R^2. Consequently, the fittings of the experimental data match perfectly to the cube rate law as $R^2 = 0.999$ for both alloys. Although the fittings of the square of the average precipitate size also matches well to the square rate law, the R^2 values are slightly lower compared to those of the cube rate law. The matrix-diffusion controlled coarsening rate, which is determined by cube rate law, is 9.30 nm^3·s^{-1} and 4.69 nm^3·s^{-1} for alloys 0Re5Ta and 2Re5Ta, respectively. Likewise, the interface-diffusion controlled coarsening rate, which is determined by square rate law, is 0.0179 nm^2·s^{-1} and 0.0093 nm^2·s^{-1} for alloys 0Re5Ta and 2Re5Ta, respectively. Obviously, alloy 0Re5Ta has a coarsening rate that is nearly double that of alloy 2Re5Ta, regardless which model is considered.

Multivariate non-linear regression analysis was also employed to determine the accurate temporal exponents n and the corresponding coarsening rate, as shown in Fig. 4. This was done without assuming the constant $n=3$ as indicated in the P-V model developed for multi-component alloys. The non-integer temporal exponent n and optimized regression parameters t_0, $R(t_0)$ and k are listed in Table 3, including the uncertainties as the standard error in the regression. The non-linear regressions refer to a goodness of fit as χ^2, attached in Fig. 4. The non-linear regressions yield temporal exponents of 2.82 and 2.74 for alloy 0Re5Ta and alloy 2Re5Ta, respectively, indicating a diffusion-limited coarsening in both alloys since the temporal exponents approach the prediction of 3 for quasi-steady-stationary coarsening from the LSW

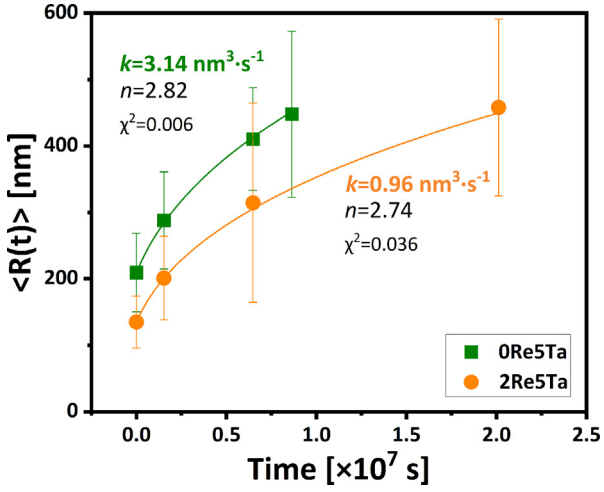

Fig. 4. Plots of the average precipitate radius, $R(t)$ versus thermal exposure time, giving the non-integer temporal exponent n and the corresponding coarsening rate k by multivariate non-linear regression analysis.

theory for binary system [13–15], K-V model for ternary system [18] as well as P-V model for multi-component system [19]. A lower n value away from 3 can be found in alloy 2Re5Ta, indicating a closer tendency towards interface-diffusion controlled coarsening within even longer duration. The related coarsening rates are 3.14 nm^3·s^{-1} and 0.96 nm^3·s^{-1} for alloy 0Re5Ta and alloy 2Re5Ta, respectively. As shown in Table 3, within non-linear regression analysis, the time for the onset of quasi-stationary coarsening, t_0, is optimized as a value much close to zero, meanwhile the $R(t_0)$ also approaches the measured radius at the initial state of each alloy, both indicating the quasi-stationary coarsening starts from the quite initial state. It is clear that the addition of Re can effectively and substantially slow down the coarsening behavior, regardless of which theory or model is applied.

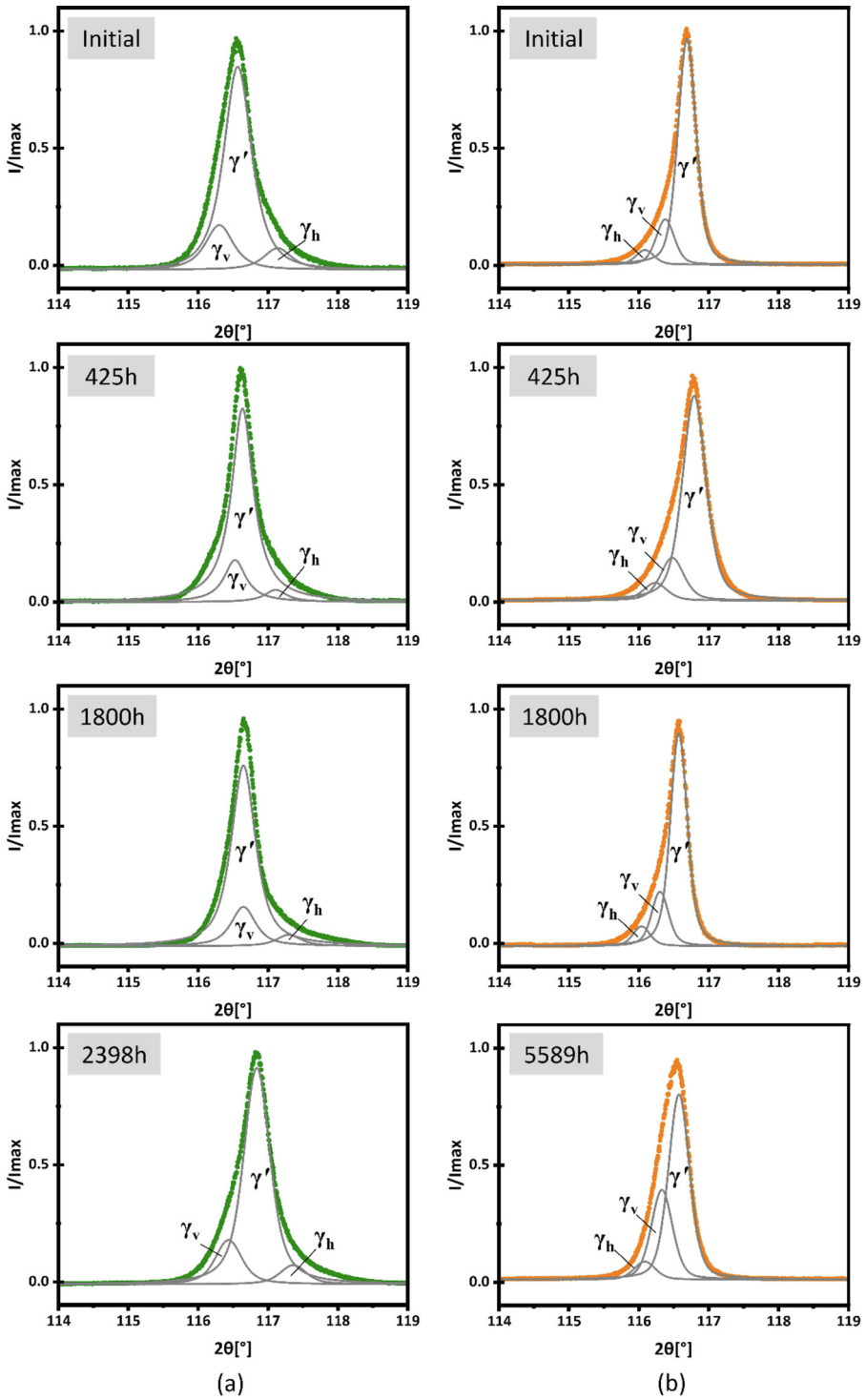

Fig. 5. X-ray diffraction profiles of the (004) reflections at 900 °C on the initial samples and on the samples after thermal exposure for different durations of (a) alloy 0Re5Ta and (b) alloy 2Re5Ta. The sub-peaks for γ' precipitates and vertical (γ_v) and horizontal (γ_h) matrix are also included.

3.3. Lattice misfit between γ and γ' phases

The (004) two-phase reflection was chosen for deconvolution and determination of the lattice parameters of the γ and γ' phases, as high-order peaks provide much better signal-to-noise ratio and exhibit higher detected data accuracy guided by the Bragg function, as well as more sufficient peak splitting than low-order peaks [38]. Fig. 5 shows the (004) diffraction reflections of the experimental samples recorded at 900 °C. The sharp diffraction peaks indicate a strong overlap between the individual phases, i.e. a low misfit. The highly asymmetric (004) reflections of alloy 0Re5Ta reveal the closeness of the lattice parameters of γ and γ' phases, while for alloy 2Re5Ta, the moderate slope on the low-angle site of the peak indicates an apparent negative lattice misfit for all conditions. This is consistent with our previous post-creep (subjected to long-term creep at 900 °C/200 MPa) microstructural results, showing that alloys 0Re5Ta and 2Re5Ta possess P-type and N-type rafting morphology, respectively, due to

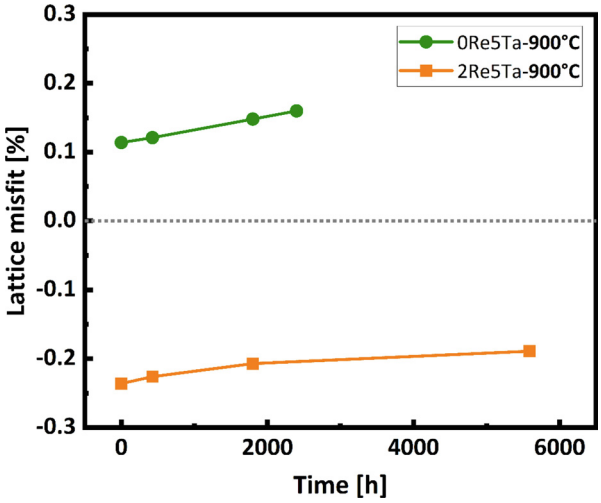

Fig. 6. Evolution of the calculated lattice misfit as a function of thermal exposure time of alloys 0Re5Ta and 2Re5Ta measured at 900 °C.

the positive misfit of alloy 0Re5Ta and negative misfit of alloy 2Re5Ta [11].

The sub-peaks representing γ' phase and vertical (γ_v) and horizontal (γ_h) channels are shown in Fig. 5, indicating the increasing area under the γ sub-peaks over time, with regard to the decreasing γ' volume fraction during thermal exposure, which is consistent with the measured tendency from the microstructural observation for both alloys. Fig. 6 shows the calculated lattice misfits as a function of time. In alloy 0Re5Ta, the two sub-peaks of the γ phase are located at the opposing sides of the γ' peak, deriving a near-zero lattice misfit of 0.114% in the initial state. During long-term thermal exposure, the total fraction of the γ phase increases, as some of γ' phase dissolves. The positive misfit of alloy 0Re5Ta increases its magnitude over time, leading to a larger lattice misfit after long-term thermal exposure. In contrast, in alloy 2Re5Ta, the two sub-peaks of the γ phase are located on the left side of the γ' peak, leading to a considerable negative lattice misfit of -0.236% in the initial state. As the thermal exposure time increases, the total fraction of γ phase also increases, again indicating substantial dissolution of γ' phase in alloy 2Re5Ta. The calculated lattice misfits of alloy 2Re5Ta in Fig. 6 also show an increasing tendency over time, yet the magnitude of the lattice misfit decreases and tends to zero at longer durations.

3.4. Elemental partitioning across the γ/γ' interface

To explore the direct consequence of mass transport across the γ/γ' interface as the particles coarsen during the thermal exposure, multiple atom probe measurements were carried out on samples in the initial state and at different thermal exposure durations for both alloys. Fig. 7(a) presents a 3D reconstruction of a selected result (alloy 2Re5Ta after thermal exposure for 5589 h) containing an interface marked by 15 at.% Cr iso-concentration surface. Al atoms (in red) and Cr atoms (in blue) are displayed as they are strongly partitioning elements and represent γ' precipitate and γ matrix, respectively. Here, W does not show any obvious tendency towards a single phase in the ion distribution map. Compositional profiles obtained from proxigrams were used to determine the average composition in far-field and the local characteristics through the γ/γ' interface, adjusting for any peak overlaps of the elemental isotopes based on their natural abundancies [39]. The partitioning coefficient $K_i^{\gamma/\gamma'}$ was used to quantitatively describe the partitioning behavior of alloying elements between the phases, and is defined as

$$K_i^{\gamma/\gamma'} = C_i^{\gamma}/C_i^{\gamma'} \quad (4)$$

where C_i^{γ} and $C_i^{\gamma'}$ represent the atomic concentration of a selected element i in γ and γ' phases, respectively. For better representation of the partitioning, a logarithmic form of the coefficient for each element in the initial state and at the longest duration for the two experimental alloys is taken and plotted in Fig. 7(b). Here, the columns towards left (right) indicate that the element partitions to γ' (γ) phase, showing a further confirmation that a more drastic partitioning occurs for almost all of the elements after long-term thermal exposure for both alloys.

There is slight tendency for W to partition to γ matrix in the initial state of both alloys, Fig. 7(b). However, the partitioning behavior changes after prolonged time, such that W becomes more enriched in γ' precipitates. To clearly illustrate this, the continuous evolution of the partitioning behavior of W during thermal exposure is shown in Fig. 8, and the partitioning coefficient calculated by Eq. (4) is also included. The results indicate an inversion of the partitioning behavior of W towards γ' precipitates (with partitioning coefficient lower than 1) beyond 425 h for both alloys. We also observed a similar W partitioning behavior after creep at 900 °C for both alloys [11]. In contrast, for traditional multi-component Ni-based alloys, W generally partitions to the γ matrix with partitioning levels increasing during the prolonged thermal exposure [40]. Thus, the change in partitioning behavior of W is a special phenomenon for this alloying system and needs to be explored further.

4. Discussion

4.1. Microstructural and mechanical response to the lattice misfit and solute partition

During stress-free thermal exposure at high temperatures, it is commonly believed that the γ' morphology evolution can be attributed to the combination of the elastic strain-energy and interfacial energy, and has been evidenced by numerical results carried out for multiple particles [41,42]. The elastic strain field induced by the lattice misfit between the γ matrix and coherent γ' precipitates provide the driving force for the formation of cuboidal γ' precipitates with the lowest strain energy after heat treatment. As shown in Figs. 2 and 6, the addition of Re results in a decrease of the lattice misfit from 0.114% to -0.236%, leading to more cuboidal γ' precipitates at the initial state. Meanwhile during thermal exposure, the interfacial energy (or minimization of) promotes coarsening and γ' precipitates evolve towards spherical morphology in order to minimize the specific surface area. However, in alloy 0Re5Ta, the progressively increasing magnitude of the lattice misfit promotes a more cuboidal morphology of γ' phase. In general, γ' precipitates tend to be nearly-spherical in morphology when the lattice misfit is close to zero, but as the absolute value of the lattice misfit increases, the γ' phase progressively evolves into a more cuboidal morphology, regardless of the lattice misfit sign [12]. The evolution of the absolute value of lattice misfit is proportional to the shape parameter listed in Table 2.

The unconstrained lattice parameters of γ and γ' phases can be closely linked to the phase compositions [43]. The partitioning behavior of these two SX superalloys shows an obvious shift after long-term evolution compared to that after the full heat treatment, indicating the increasing partitioning preference over time. This tendency is in agreement with many other alloying systems like Ni-Al-Cr-W-Re alloy [44] and Co-Al-W-Ni alloy [45]. The inversion of the partitioning behavior of W from a slight preference to γ matrix after full heat treatment to a stronger preference to γ' precipitates during thermal exposure is a special phenomenon

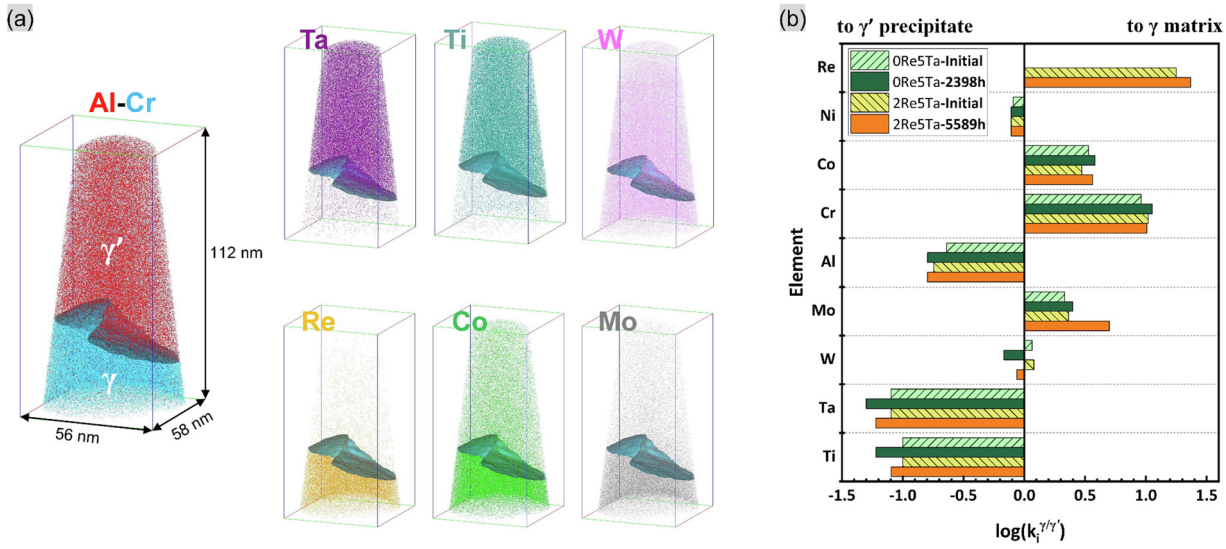

Fig. 7. (a) A reconstruction of an associated APT tip of alloy 2Re5Ta containing a phase interface presented by 15 at.% Cr iso-concentration and the ion distribution map for every major element; (b) elemental partitioning coefficients $\log(K_i^{\gamma/\gamma'})$ between γ and γ' phases at initial state and after the longest thermal exposure time for both alloys.

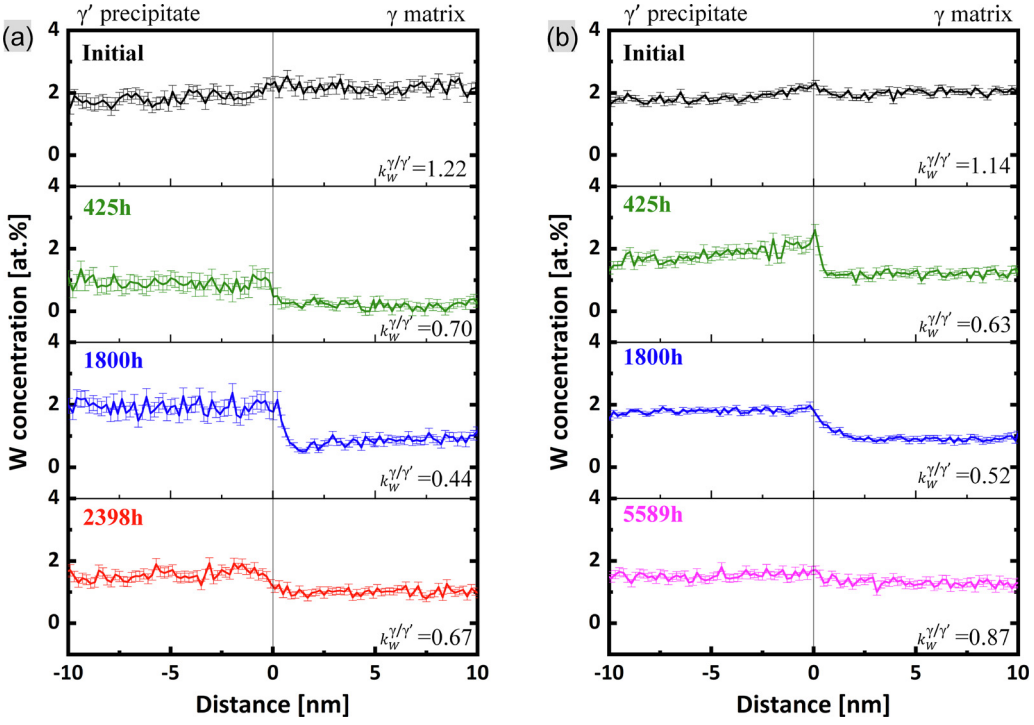

Fig. 8. The concentration profile of element W across the γ/γ' interface during thermal exposure for different durations at 900 °C for (a) alloy 0Re5Ta and (b) alloy 2Re5Ta. The calculated partitioning coefficients are also included.

in this experimental alloying system. This inversion is different from observations in other alloying systems where W partitions more strongly towards the γ matrix in multi-component alloys as driven by Ta additions [40,46]. As illustrated in Fig. 8, W reaches the strongest partitioning towards γ' phase at 1800 h for both alloys. This inversion in W partition contributes to the significant increase of the γ' lattice parameter, leading to a stronger separation between the lattice parameters of γ and γ' phases for alloy 0Re5Ta and approaching lattice parameters of γ and γ' phases for alloy 2Re5Ta, respectively, considering the opposite sign of lattice misfit. This observation gives a direct but non-quantitative insight that the inversion of the W partitioning behavior along with the diffusion of other elements results in an opposite evolution tendency of the lattice misfit of the two alloys, as shown in Fig. 6.

To illustrate the effect of the W partitioning, Fig. 9 shows the measured nano-hardness of alloy 2Re5Ta for the two-phase microstructure and just for γ' phase (due to the size of the γ channels, a measurement of the γ nano-hardness was not possible). The nano-hardness of the crept specimen from Ref. [11] is also measured for comparison, since smaller partitioning coefficients (except for W) were found after creep. Notably, the thermal exposure test was conducted for the same duration as the creep test, and the γ' volume fraction of the two conditions is very similar. Multiple measurements were taken for each alloy's two-phase microstructure and its γ' phase, and are represented as the black dots

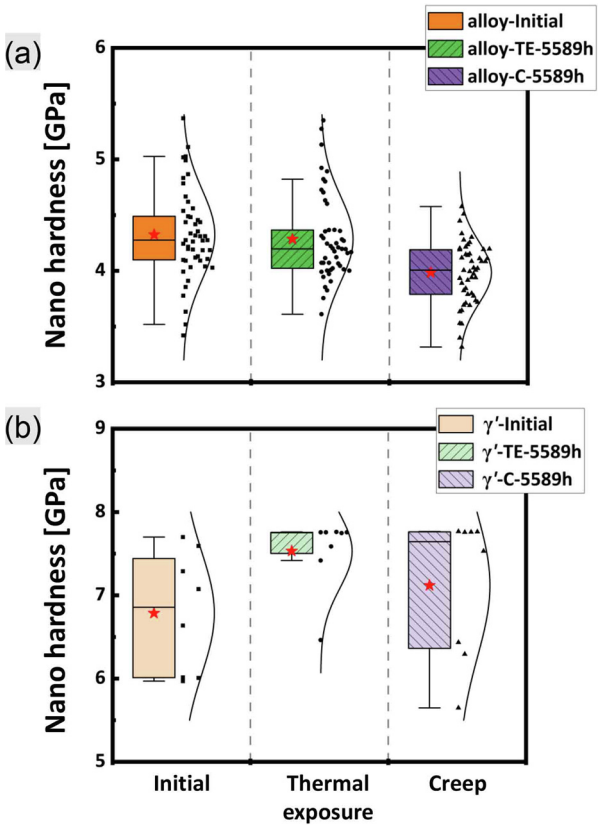

Fig. 9. Measured nano-hardness of (a) alloy 2Re5Ta and (b) its single γ' phase at the initial state and after thermal exposure and creep for 5589 h (the red stars refer to the average of each series data).

in the plots, along with the normal distribution curves and the average values (red stars). Although the total hardness of the two-phase microstructure is reduced after thermal exposure or creep, as shown in Fig. 9(a), the γ' hardness is increased in Fig. 9(b), especially for the specimen after thermal exposure, which possess increasing partitioning coefficients of Al, Ti and Ta combining with the inversed W towards γ' phase. Stress changes the partitioning of elements, inducing smaller partitioning coefficients after creep, rather than the bigger partitioning coefficients after thermal exposure [11]. Interestingly, the γ' hardness is still enhanced slightly despite decreasing partitioning coefficients after creep, providing evidence of the strengthening effect due to the W partitioning inversion towards γ' phase.

4.2. Calculation of the γ/γ' interfacial energy

Thermodynamically, the interfacial energy which arises from the precipitate-matrix boundary mismatch, acts as the driving force for coarsening and hence controls the microstructural stability [47]. Coarsening is usually the result of the minimization of interfacial energy with the time, i.e. the so-called Ostwald ripening process [48]. In recent years, the development of APT has allowed for the precise determination of the interfacial width and composition over a distance at the near-atomic scale. On this basis, Ardell developed an approach to calculate the interfacial energy from the compositional gradient across the γ/γ' interface as proposed by Cahn and Hilliard [20,49]. The interfacial energy, σ, is defined as:

$$\sigma = 2\int_{C_i^{\gamma}}^{C_i^{\gamma'}} \left(\frac{\chi \cdot \Delta G_m}{V_m}\right)^{1/2} dC \tag{5}$$

where ΔG_m is the change in molar free energy towards an equilibrium mixture of γ and γ' and V_m is the molar volume of γ' precipitates. These two parameters can be computed by Thermo-Calc thermodynamic computational software within the TCNi9 database [50]. The gradient energy coefficient, χ, is of crucial role in the selection of composition modulations for growth or dissolution, and can be calculated from:

$$\Delta G_m = \chi \cdot V_m \cdot \left(\frac{dC}{dz}\right)^2_{max} \tag{6}$$

where $(\frac{dC}{dz})_{max}$ is calculated by the maximum slope of the concentration profile at the γ/γ' interface. By substituting of Eq. (6) into Eq. (5) and adopting the APT interfacial results into the sigmoid function as described in detail in Refs. [20,24], the interfacial energy, σ, can be easily calculated by:

$$\sigma = \frac{\chi \cdot \eta \cdot \Delta C_i^2}{3} = \frac{4}{3} \cdot \frac{\chi \cdot \Delta C_i^2}{\lambda} \tag{7}$$

where ΔC_i is the concentration difference between γ and γ' phases, λ is the interfacial width determined by APT and measured by the approach outlined by Cahn [49] and Ardell [20]. To be mentioned here is that the APT results for determining the interfacial features are from the samples thermally exposed for 1800 h in both alloys, which offers good comparison between the alloys and a good agreement with the matrix-diffusion model which is discussed in detail in Section 4.4. The interfacial parameters, including the interfacial width λ, the compositional gradient $(\frac{dC}{dz})_{max}$ and the concentration difference between γ and γ' phases were calculated from the proxigrams with respect to the Al iso-concentration surface, since Al is the most proper element to form the Ni_3Al precipitates and shows an obvious concentration difference through the γ-Ni/γ'-Ni_3Al interface. Consequently, the interfacial energies of alloys 0Re5Ta and 2Re5Ta were calculated as 50.2 mJ·m^{-2} and 25.2 mJ·m^{-2}, respectively, as listed in Table 4. Alloy 0Re5Ta possesses twice the interfacial energy of alloy 2Re5Ta, which provide a stronger driving force for coarsening. For a further clarification, the interfacial energy is also conducted by the interfacial parameters of other elements Ti, Ta, Cr and Co, which is listed in Appendix A, and more detailed information confirming Al as the most appropriate element to determine the interfacial energy by Ardell's method is also attached.

However, there might be additional contributions to the interfacial energy since the alloying elements in multi-component systems introduce complexity to the γ/γ' heterophase interface. Thus, the P-V model provides a generalized treatment of the coarsening kinetics for multi-component alloys to estimate their interfacial energy. The P-V model yields a coarsening rate constant by an analytic equation [19]:

$$k_{PV} = \frac{8V_m^{\gamma} \cdot \sigma}{9\left(\Delta\bar{\mathbf{C}}\right)^T \mathbf{M}^{-1} \Delta\bar{\mathbf{C}}} \tag{8}$$

where V_m^{γ} molar volume of γ matrix, $\Delta\bar{\mathbf{C}}$ and $(\Delta\bar{\mathbf{C}})^T$ are the concentration and transposed concentration vector, $\mathbf{M}^{-1}$ is the inverse of the mobility matrix **M,** which is defined by $\mathbf{D} = \mathbf{M}\mathbf{G}^{\gamma}$ (herein **D** is the diffusivity matrix and $\mathbf{G}^{\gamma}$ is the Hessian of the Gibbs free energy of the γ phase, that is $\mathbf{G}^{\gamma} = G_{\gamma,ij}$). The P-V model uses a volume-fixed frame of reference. The appropriate mobility term **M**, with $\mathbf{G}^{\gamma}$ the potential gradient of interest, can be written as the symmetric matrix L''_{ki}:

$$L''_{ki} = \sum_{j=1}^{n}\sum_{r=1}^{n} (\delta_{ir} - C_i)\left(\delta_{jk} - C_k\right)L_{ir} \tag{9}$$

where $L_{ij} = \delta_{ij}C_iM_i$. $\delta_{ij} = \begin{cases} 1 & (i = j) \\ 0 & (i \neq j) \end{cases}$ is the Kronecker delta. M_i is the temperature-, composition-, and pressure-dependent atomic

Table 4
Interfacial parameters determined by the APT compositional profiles across the flat γ/γ' interfaces of the samples after thermal exposure for 1800 h as well as the calculated interfacial energy by Ardell's method based on Al for alloys 0Re5Ta and 2Re5Ta.

Alloy	Ardell's method				P-V model
	λ [nm]	$(\frac{dC}{dz})_{max}$ [at.%·nm^{-1}]	ΔC_{Al} [at.%]	σ [mJ·m^{-2}]	σ [mJ·m^{-2}]
0Re5Ta	2.87	10.31	12.42	50.2	60.3
2Re5Ta	2.65	16.02	12.76	25.2	30.0

*Note: The interfacial energy determined by P-V model is also listed here.

mobility of component i, which can be acquired in the Thermo-Calc MOBNI5 mobility database [50]. The mobility matrix L''_{ki} calculated at 900 °C for the γ-matrix compositions determined via APT for alloys 0Re5Ta and 2Re5Ta are given in Appendix B. Here, the dimension of the coarsening rate k_{PV} should be inaccurate since the non-integer temporal exponent n. While due to the diffusion-limited coarsening in both alloys with the temporal exponent close to 3, it can be simplified as an accurate dimension for the possible estimation of the interfacial energy in P-V model. Consequently, they were determined as 60.3 mJ·m^{-2} and 30.0 mJ·m^{-2} for alloy 0Re5Ta and alloy 2Re5Ta, respectively (also shown in Table 4). These results also demonstrate that the interfacial energy of alloy 0Re5Ta is twice that of alloy 2Re5Ta.

Stemming from the basic diffusion-limited coarsening theory, the P-V model provides analogical results for the interfacial energy as that by Ardell's method, despite the classical LSW theory assuming a dilute binary alloying system. The interfacial energy calculated by the P-V model is higher than that from Ardell's method, indicating that there are additional contributions to the interfacial energy other than the compositional gradient. These may be attributed to the complex interfacial features introduced by the alloying elements with distinct atomic radii, however, this cannot be estimated quantitatively yet. More importantly, Re, as the most effective element to control the diffusion and enhance the microstructural stability during the creep of Ni-based superalloys [51,52], would delay the coarsening kinetics in this alloying system.

4.3. Elemental dependence of the coarsening rate

Although the LSW theory was derived based on binary alloying systems with some limited conditions, it is still widely and successfully applied to multi-component alloys. One of the main reasons for the limitation lies in the use of the Gibbs-Thomson equation, which is the core of the coarsening theory. For a binary alloying system, the Gibbs-Thomson equation relate the interfacial curvature with interfacial composition, which is determined by the local equilibrium originating from the interfacial chemical potential. However, for multi-component alloys, the local interfacial equilibrium composition cannot adequately describe the interfacial features, and further interfacial characteristic besides the interfacial composition should be considered. Thus, Kuehmann and Voorhees [18] modified the Gibbs-Thomson equation with the consideration of the complex diffusion behavior, especially through the precipitate-matrix heterophase interface. The modified LSW theory, which is more appropriate for multi-component alloys, provides the corresponding relationship between the coarsening rate and diffusivity of a single element [13,18,53]:

$$k = \frac{8}{9} \cdot \frac{D_s \cdot \sigma \cdot V_m \cdot C_i^{\gamma} \cdot \left(1 - C_i^{\gamma}\right)}{R \cdot T \cdot \left(C_i^{\gamma'} - C_i^{\gamma}\right)^2} \tag{10}$$

where R is the universal gas constant, T is the absolute temperature, D_s is the effective diffusivity of the selected element in γ matrix, which can be obtained by the approach of Zhu et al. [54] utilizing the activation energy and the pre-exponential factor for each element, as listed in the first line of Table 5. Although it is not the best model for multi-component alloys, it can provide good guidance on the determination of the rate-limiting element by using the diffusivity for a single element. When taking the interfacial energy as a constant, as it should be, one single element can lead to a similar analytical coarsening rate with the regressive one, i.e., that is the most important element which makes the overall diffusivity as if it contains only one element, so-called "rate-limiting element".

The different calculated k values for the two alloys based on the diffusivity and compositions in γ and γ' phases for each element are also listed in Table 5. For a direct comparison, the measured coarsening rate from the particle size analysis (when $n = 3$) in Section 3.2 are tabulated in the second column of Table 5. Here, the interfacial energy obtained from the P-V model and Ardell's method are both used for comparison. For alloy 0Re5Ta, Cr acts as the element which provides the closest calculated k (8.31 nm^3·s^{-1}) to the fitted k (9.30 nm^3·s^{-1}) when adopting the interfacial energy by Ardell's method, and by P-V model ($k = 9.98$ nm^3·s^{-1}). This is related to three considerations. First, Cr is the primary alloying addition, with 10 wt.% in nominal composition. Second, since we consider the main controlling mechanism to be matrix-diffusion, the elements that partition to γ matrix are more likely to control the diffusion process. Third, Cr is strongly partitioned to γ matrix with a coefficient of over 10, which is incomparably higher to all other elements. In addition, Cr has been shown to enhance the partitioning behaviors of other elements in both Ni-based and Co-based superalloys, which lead to the increased saturation degrees of the solid solution elements in γ matrix [55,56]. The most recent research on CoNi-based superalloys with high Cr content also demonstrated that Cr, as the rate-limiting element, can be helpful for decreasing the coarsening rate [57]. These evidences contribute to the reliability for Cr to be determined as the rate-limiting element in the current alloying system. Analogously, for alloy 2Re5Ta, Re should undoubtedly be the rate-limiting element as it has the lower diffusivity in both phases and strong partitioning extent between the two phases. Indeed, the calculated k based on Re (4.62 nm^3·s^{-1}) is the closest to the fitted k (4.69 nm^3·s^{-1}), whilst the calculated k based on Cr (4.29 nm^3·s^{-1}) is also within the same magnitude, when adopting the interfacial energy by Ardell's method. With the interfacial energy from the P-V model, the calculated k based on Cr (5.11 nm^3·s^{-1}) is the closest to the fitted one and that based on Re (5.50 nm^3·s^{-1}) also doesn't differ too much. It can thus be deduced that Cr gives priority to limit the coarsening rate in the Re-free alloy, while Re and Cr can both act as the rate-limiting element in the Re-containing alloy, with slight compositional changes leading to the favoring of one over the other. With the addition of Re, the diffusion of other elements is retarded, as represented by the change of elemental partitioning coefficient in a smaller range despite a longer duration shown in Fig. 6(b), and the effective decrease of coarsening rates calculated by the diffusivity of other elements, as shown in Table 5.

Table 5
Effective diffusivity of specific elements in the γ matrix and the coarsening rates determined by the experimentally measured precipitate sizes and calculated based on interfacial parameters (σ from different methods) and diffusivity of the comprising elements.

	By regression ($n=3$)	Al	Ti	Cr	Co	Ta	Re	W	Mo	Method*
D [$*10^{-18}$m^2·s^{-1}]		760	258	70.2	15.1	145.5	3.61	14.0	34.2	
$k_{(0Re5Ta)}$	9.30	37.86	11.96	8.31	5.01	11.46	–	208	776	Ardell
[nm^3·s^{-1}]		45.48	13.76	9.98	6.02	14.36	–	250	933	P-V
$k_{(2Re5Ta)}$	4.69	19.71	8.75	4.29	2.63	7.06	4.62	901	91.1	Ardell
[nm^3·s^{-1}]		23.47	8.40	5.11	3.13	10.42	5.50	1073	108	P-V

* *Note*: method refers to the adapted interfacial energy in Eq. (10) originating from the specific coarsening model.

Due to the prolonged service times, the design strategy for alloys used in IGT applications aims to achieve a near-zero lattice misfit and low interfacial energy in order to inhibit the coarsening kinetics and extend the high temperature strength during service [2,58]. Therefore, it is beneficial to add Re, which enhances the solid solution strength of the matrix and slows down the overall effective diffusion [59,60], and to decrease Ta, which contributes to the minimization of the lattice misfit [61]. Although W also exhibits a large atomic radius and low diffusivity in both phases, it does not act as the rate-limiting element as it does not partition as strongly as Re and Cr. Despite the lower lattice misfit of 0Re5Ta, it is recognized that both of the microstructural stability and the high temperature mechanical performance cannot compare with that of alloy 2Re5Ta; this was confirmed in our previous study [11].

4.4. Competition between matrix-diffusion controlled and interface-diffusion controlled coarsening

The coarsening mechanism can be mainly described by two microscopic kinetic processes: matrix-diffusion controlled (MDC) and interface-diffusion controlled (IDC) mechanisms. It has been shown that different coarsening controlling mechanisms directly contribute to the coarsening behaviors of the particle growth and the particle size distribution (PSDs) [23]. In Fig. 3, the linear fitting has been conducted for the case of $n=3$ and $n=2$. While in Fig. 4, non-linear regression analysis has been conducted to determine the non-integer temporal exponent, n, which was determined as 2.82 and 2.74 for alloys 0Re5Ta and 2Re5Ta, respectively. These indicate the coarsening kinetics is co-controlled by MDC and IDC mechanisms simultaneously along with the whole coarsening process for both alloys, and a higher tendency towards IDC diffusion in alloy 2Re5Ta. Considering the overall coarsening process is in a quasi-stationary state with approximately constant γ' volume fraction, thus, comparing the PSDs from experimental data with that predicted by the different coarsening theories is an effective approach to distinguish the dominant mechanism during the long-term coarsening process.

Although there are many modified expressions to fit the PSDs for multi-component alloys with high precipitate volume fraction, we only consider the extreme cases for $n=3$ (presented in classical LSW theory) and $n=2$ (presented in TIDC theory), since the exponent n lies in the range of 2-3, and the PSDs obtained by the Monte Carlo approach always lays between these extremes [62]. Although the LSW theory has been developed for simple alloys, it has been widely adapted to also describe the Ostwald ripening of modern superalloys [7,63]. Meanwhile, as the TIDC theory does not consider the effect of equilibrium volume fraction, the application of the PSDs is very useful. These two models result in different shapes of the PSDs, as described by the predicted function $g(u)$ in the LSW and TIDC model:

$$g_{LSW} = \frac{81}{2^{\frac{5}{3}}} \cdot \frac{u^2}{(1.5-u)^{\frac{11}{3}}} \cdot \frac{1}{(3+u)^{\frac{7}{3}}} \cdot e^{-\frac{u}{1.5-u}} \quad (u < 1.5) \tag{11}$$

$$g_{TIDC} = \frac{24u}{(2-u)^5} \cdot e^{-\frac{3u}{2-u}} \quad (u < 2) \tag{12}$$

Comparing the PSDs curves after different thermal exposure durations can provide insight into the time-dependent kinetics and whether there is a transition from one coarsening mechanism to another. Balden et al. [63] suggested that a good correspondence exists between the measured PSDs and the prediction given by the LSW theory after short ageing time. Sun [23] found that different coarsening mechanisms, in terms of the matrix-diffusion and the interface-diffusion, could compete in controlling the coarsening kinetics not only in different alloy system, but also at different duration over the prolonged ageing time within a single alloy. Recently, Zhang et al. [24] also experimentally showed a gradual evolution in the coarsening controlling mechanisms from matrix-diffusion controlled to interface-diffusion controlled in a multi-component Re-containing SX superalloy. When the coarsening is controlled by matrix-diffusion (Eq. (11)), the PSD curve is narrow and sharp, while interface-diffusion controlled coarsening (Eq. (12)) results in a broad and flat PSD curve. To this end, the experimental PSDs for the samples in the initial state and after different thermal exposure durations at 900 °C are shown in Fig. 10, accompanied by the predictions of the MDC mechanism (presented by LSW model, Eq. (10)) as a red solid line and IDC mechanism (presented by TIDC model, Eq. (11)) as a blue dashed line. For alloy 0Re5Ta, the PSDs are entirely consistent with the prediction by the MDC mechanism up to 1800 h, and a change towards the prediction by the IDC mechanism becomes apparent at 2398 h. In contrast, the PSDs for alloy 2Re5Ta are well described by the prediction of the MDC mechanism for short thermal exposure up to 425 h, but for 1800 h and above, the IDC mechanism fits the PSDs data much better. At 5589 h, the PSD is well-described by the prediction of the IDC mechanism, although the coalescence of particles results in wider PSD. This widening is skewed to the right with lengthening of the right tail, hence it is reasonable to assume that the result may be due to another change in the coarsening mechanism towards particle coalescence. It should be noted that the results demonstrate a gradual transition but not quantitative description between the two coarsening mechanisms, which further the notion that a single diffusion-controlled mechanism is not the only operative one for the period of time, but rather the dominant mechanism.

In short, the competition between the MDC and IDC mechanisms during the long-term coarsening process is clearly observed for both alloys. Initially, the precipitate coarsening behavior is controlled by matrix-diffusion, but it gradually transitions to interface-diffusion for prolonged time. Although the addition of Re postpones the diffusion and reduces the coarsening rate, the transition to the interface-diffusion controlled mechanism occurs earlier in alloy 2Re5Ta than alloy 0Re5Ta. Then, the coarsening is also influenced by precipitate coalescence at very long times.

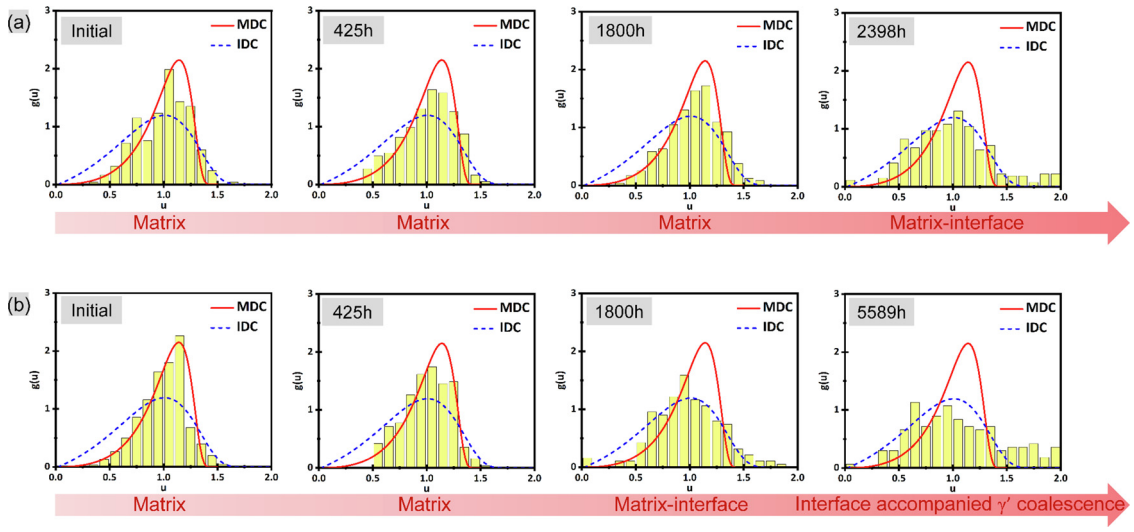

Fig. 10. PSDs of γ' precipitates during thermal exposure for different durations at 900 °C for (a) alloy 0Re5Ta and (b) alloy 2Re5Ta compared with the coarsening-controlled predictions of MDC mechanism (red solid line) and the IDC mechanism (blue dash line).

4.5. Effect of the trans-interface coarsening mechanism

In Section 4.4, it is demonstrated that the mechanism governing the coarsening behavior of the Re-containing alloy changed earlier to the interface-diffusion controlled mechanism as represented by the TIDC model, despite the reduced trans-interface coarsening rate. The value of the coarsening rate, k, proposed by the TIDC model can be calculated as:

$$k = \frac{32}{81} \cdot \frac{\tilde{D} \cdot l_y}{\Delta C_i \cdot \lambda} \tag{13}$$

where l_y is the capillary length which can be obtained from the formula presented by Ardell et al. [21,64], ΔC_i is the elemental concentration difference between γ and γ' phases. Here, Al was also used in simulation for the reason indicated in section 4.2. λ is the interfacial width determined by the 1D compositional profiles from the APT results. Based on the k values calculated by linear fitting with the temporal exponent of 2 in Section 3.2, the effective diffusion coefficient across the interface, $\tilde{D}$, can be thus calculated. Consequently, the effective trans-interface diffusion coefficients for alloys 0Re5Ta and 2Re5Ta are 6.50 $\times$ 10^{-17} $m^2 \cdot s^{-1}$ and 6.98 $\times$ 10^{-17} $m^2 \cdot s^{-1}$, respectively. The diffusion coefficients of Al in γ-Ni and γ'- Ni_3Al are 7.60 $\times$ 10^{-16} $m^2 \cdot s^{-1}$ [65] and 6.47 $\times$ 10^{-17} $m^2 \cdot s^{-1}$ [66] within the binary Ni-Al system, respectively. Although the diffusion coefficient of Al would be affected in multi-component alloys, the calculated trans-interface diffusion coefficients for alloys 2Re5Ta and 0Re5Ta still lie between that of Al in γ-Ni and γ'- Ni_3Al. The trans-interface diffusion coefficients for both alloys are closer to that in γ' phases with lower diffusion coefficient, indicating that once the dominant mechanism change from MDC to IDC, the diffusion coefficients which play the rate-controlling role tend to decrease, and the coarsening process can be further slowed down when the coarsening is dominated by interface diffusion.

Although alloy 2Re5Ta has a slightly higher trans-interface diffusion coefficient, it still has a considerably lower coarsening rate in the TIDC model calculated in Section 3.2. Apart from $\tilde{D}$, the interfacial width λ is another important parameter affecting the coarsening rate. Fig. 11 shows the evolution of the interfacial width during thermal exposure for the two alloys. It was estimated by measuring the horizontal distance between the 10% and 90% of the plateau matching the far-field concentrations of the γ and γ' phase. The measured interfacial width $\lambda(t)$ and the normalized interfacial width $\lambda(t)/\langle R(t)\rangle$ versus the mean precipitate radius and thermal exposure time are displayed in Fig. 12. The interfacial widths in the initial state are nearly the same for both alloys, and both the interfacial width and normalized interfacial width decrease over time. Since an inverse relationship holds between k and λ values, the trans-interface coarsening rate plays an increasingly important (and gradually more dominant) role in the coarsening behavior. In alloy 0Re5Ta, the interfacial width decreases slightly for a long period, however, alloy 2Re5Ta decreases its interfacial width more rapidly and exhibits a sharper interface up to 1800 h, Fig. 11(b). This implies that the interface-diffusion controlled mechanism becomes more dominant earlier in alloy 2Re5Ta rather than alloy 0Re5Ta. However, after prolonged thermal exposure time for 1800 h, the interfacial width of alloy 0Re5Ta decreases rapidly to 1.91 nm at 2398 h, while alloy 2Re5Ta decrease its interfacial width to 2.42 nm even after longer thermal exposure time of 5589 h. The delayed decrease of the interfacial width in alloy 2Re5Ta may be attributed to the considerable coalescence of γ' precipitates in order to decrease the interfacial area during the coarsening process.

In addition, the normalized interfacial widths of both alloys approach zero, i.e. a sharp interface, but still retain a certain value for both alloys up to the longest thermal exposure time, indicating that the interfacial width does not become atomically sharp. The decreasing interfacial width with thermal exposure time is opposite to the ansatz in the TIDC coarsening model which predicted that the interfacial width increase with increasing time as well as the precipitate sizes [62]. However, similar observations on the decrease of the interfacial width with thermal exposure time has been demonstrated in many alloying systems studied by advanced APT, and this phenomenon has become a consensus in coarsening kinetics in recent years [29,44,67].

In this research, the Ardell's method (based on the classical LSW theory) and more recent P-V model are both applied for the determination of the interfacial energy, which is one of the key point in the discussion of coarsening kinetics. Undoubtedly, the P-V model is developed in view of the complex elemental effect and interaction, which is more appropriate for multi-component alloying systems. However, it is demonstrated that the Ardell's method, which proposes a more concise arithmetical process, can also give a value of interfacial energy similar to that simulated by P-V model, when the interfacial parameters of a proper element are chosen for the simulation for multi-component alloys.

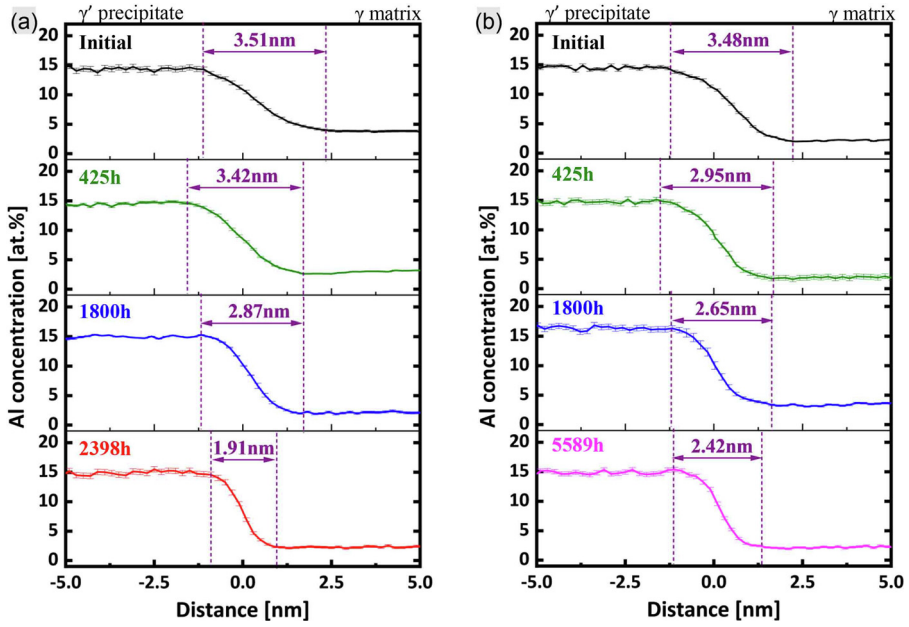

Fig. 11. Evolution of the interfacial widths during thermal exposure for different durations at 900 °C determined by the APT compositional profiles for (a) alloy 0Re5Ta and (b) alloy 2Re5Ta.

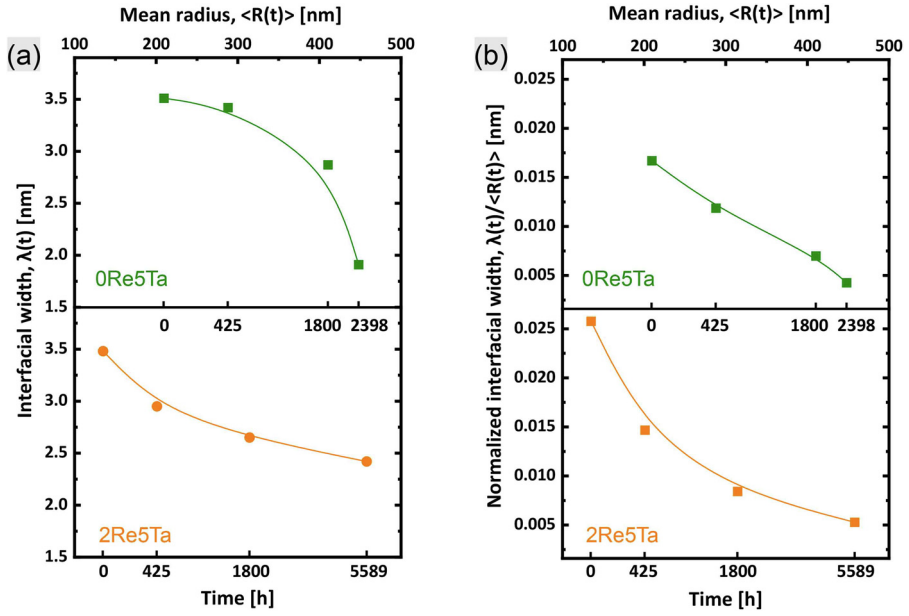

Fig. 12. The temporal evolution of (a) interfacial width λ(t) and (b) normalized interfacial width, $\lambda(t)/\langle R(t)\rangle$, as a function of mean precipitate radius and thermal exposure time.

Our present results support that the classical LSW theory, which is the solid foundation of the diffusion-controlled coarsening, can also provide an effective guidance to the coarsening kinetics for multi-component and commercial alloys, as indicated in other researches [7,68-70].

The IGT superalloys demand high microstructural stability to adapt to the relative low temperature and stress as well as the long operating times of IGT blades. In this research, it is demonstrated that the limited addition of Re leads to superior microstructural stability, which is mainly attributed to the slower elemental diffusion and the lower interfacial energy compared to the Re-free alloy. However, it cannot be neglected that Cr, as a main component in IGT superalloys, is determined to be the rate-limiting element for the coarsening process in both Re-free and Re-containing alloys. Even in other alloying systems, such as Co-based or CoNi-based superalloys, Cr is also confirmed to play an important role in the microstructural stability [56,57]. These results indicate that Cr should be paid attention to during alloy design of IGT superalloys due to its strong preference to γ matrix and subsequently considerable solid solution effect, as well as the rate-limiting effect on the γ' coarsening process.

The lattice misfit is another concerning aspect to meet the demand of high microstructural stability of IGT superalloys. Traditional knowledge preliminarily claims that a lower lattice misfit should corresponds to a better microstructural stability [2,58]. Here, superior microstructural stability has been achieved in Re-containing alloy, in spite of the negative lattice misfit with higher magnitude introduced by Re in the initial state. Nevertheless, the

lattice misfit undergoes inevitable changes during thermal exposure, and the magnitude of the lattice misfit tends to similar values after very long time for both alloys. This indicates that not just the lattice misfit in initial state should be considered in the alloy design, but the change of the lattice misfit over the whole evolution process should also be taken into account. Furthermore, the addition of Re can also change the rafting behavior with the negative lattice misfit and provide effective creep resistance during high-temperature creep in IGT superalloys [11]. Overall, the preliminarily idea that a near-zero lattice misfit leads to better microstructural stability should be further expounded - yet a certain magnitude of negative lattice misfit (at high temperature) is needed, considering both the superior microstructural stability and the enhanced creep performance required by IGT superalloys.

5. Conclusions

The Re effect on microstructural evolution of SX superalloys during long-term thermal exposure at 900 °C, i.e., alloy 0Re5Ta (for 2398 h) and alloy 2Re5Ta (for 5589 h), was thoroughly investigated and clarified by the evolution of lattice misfit and elemental partitioning behavior. The coarsening rate, interfacial energy, diffusion coefficient and particle size distributions were comprehensively considered for an enhanced understanding of the coarsening governing mechanisms. Several conclusions can be drawn as followed:

1 During thermal exposure at 900 °C, the γ' volume fraction decreases from similar value at the initial state to almost the same value at the longest times, and the γ' size increases over time as well for both alloys, although alloy 2Re5Ta undergoes longer time (>5000 h). These changes are accompanied by distinct γ' morphological evolution of near cuboidal to cuboidal for alloy 0Re5Ta and cuboidal to near spherical for alloy 2Re5Ta, attributing to the changing lattice misfit - alloy 0Re5Ta possesses positive lattice misfit with increasing magnitude and alloy 2Re5Ta possesses negative lattice misfit with decreasing magnitude during long-term thermal exposure.
2 The inversion of the W partitioning from γ phase to γ' phase contributes to the increasing γ' lattice parameter and corresponding evolution of lattice misfit combined with the increasing partitioning coefficients of other elements during thermal exposure. Despite the deteriorated strength of the whole alloy after long-term thermal exposure or creep, the evolution of partitioning behavior, especially the inversion of the W partitioning, can significantly contributes to the γ' strength, as indicated by the nano-hardness measurements.
3 The addition of Re effectively reduces the coarsening rate of γ' precipitates, regardless of fitting the coarsening datasets by linear regressions or non-linear regression. The interfacial energy conducted by traditional Ardell's method has the approaching values of that by P-V model for both alloys, indicating the markedly low diffusivity of Re plays a role in decreasing the interfacial energy, thus reducing the driving force for coarsening and improving the microstructural stability.
4 Cr was found to play an individual key role in controlling coarsening in the absence of Re for alloy 0Re5Ta due to its high content in the alloy as well as in the γ matrix with the remarkable γ/γ' partitioning behavior. Re can effectively hinder the diffusion of other elements, thus acting as the rate-limiting element in the coarsening process in combination with Cr for alloy 2Re5Ta.
5 Matrix-diffusion controlled (MDC) and interface-diffusion controlled (IDC) mechanisms exist simultaneously during the coarsening process, wherein the growth of precipitates is dominant initially by MDC mechanism and then gradually transitions to be dominant by IDC mechanism at prolonged time. The addition of Re results in a sharper interface with a rapid decreasing interfacial width during thermal exposure compared to alloy 0Re5Ta, leading to the earlier appearance of IDC mechanism. Once the coarsening is dominated by interface diffusion, the coarsening process can be further slowed down, thus contributes to the further stability of the IGT superalloys when undergoing thermal exposure for long periods.

Appendix A. Interfacial energy conducted by Ardell's method

In Section 4.2, the interfacial energy was firstly determined by Ardell's method with the interfacial parameters of the element Al. However, this simulation originates from the binary Ni-Al alloying system and the interfacial parameters of other elements should also be considered in the similar simulations for a further comparison. Here we choose the elements with considerable contents and obvious partitioning behaviors between γ and γ' phases for both alloys to simulate the interfacial energy based on different elements, as shown in Table A.1.

The simulations of the interfacial energy based on different elements indicate that the element Al is also the most reliable element to determine the interfacial energy in multi-component alloys by Ardell's method, since it provides the closest value to that by P-V model for both alloys, which provide the unique result for a single alloy. It is also suggested the Ardell's method is still an applicable and tractable method to determine the interfacial energy based on a reliable element.

Table A.1
Interfacial parameters determined by the APT compositional profiles across the flat γ/γ' interfaces of the samples after thermal exposure for 1800 h as well as the calculated interfacial energy based on Al, Ti, Ta, Cr and Co for alloys 0Re5Ta and 2Re5Ta.

Alloy	Applied element	[nm]	$\left(\frac{dC}{dz}\right)_{max}$ [at. %nm^{-1}]	ΔC [at. %]	σ mJ m^{-2}]
0Re5Ta	Al	2.87	10.31	12.42	50.2
	Ti	3.93	2.01	3.83	91.8
	Ta	3.41	0.16	1.42	2424.7
	Cr	2.43	17.32	24.01	78.4
	Co	2.65	9.04	12.72	74.3
2Re5Ta	Al	2.65	16.02	12.76	25.2
	Ti	3.80	3.64	5.40	60.7
	Ta	3.20	0.24	1.85	2019.2
	Cr	2.07	21.01	22.40	57.7
	Co	2.60	9.46	9.32	39.2

Appendix B. The mobility matrix for the estimation of interfacial energy by P-V model

The mobility matrix L''_{ki} calculated at 900°C for the γ-matrix compositions determined via APT for alloy 0Re5Ta and alloy 2Re5Ta are given in Table B.1 and Table B.2.

Table B.1
Mobility matrix, L''_{ki}, for alloy 0Re5Ta calculated at 900°C for the γ-matrix compositions determined via APT. Values are multiplied by 10^{23}, and the units are $m^2 mol\ J^{-1} s^{-1}$.

$k\backslash i$	Al	Ti	Ta	Co	Cr	Mo	W
Al	81.115	-0.277	-0.092	-16.082	-25.762	-0.260	-0.637
Ti	-0.277	5.564	0.006	-1.126	-1.823	-0.017	-0.039
Ta	-0.092	-0.006	0.914	-0.227	-0.407	-0.002	-0.003
Co	-16.082	-1.126	-0.242	142.132	-77.049	-0.526	-0.879
Cr	-25.762	-1.823	-0.407	-77.049	195.297	-0.915	-1.626
Mo	-0.260	-0.017	-0.002	-0.526	-0.915	1.481	0.002
W	-0.637	-0.039	-0.003	-0.879	-1.626	0.002	0.772

Table B.2
Mobility matrix, L''_{ki}, for alloy 2Re5Ta calculated at 900°C for the γ-matrix compositions determined via APT. Values are multiplied by 10^{23}, and the units are $m^2 mol\ J^{-1} s^{-1}$.

$k\backslash i$	Al	Ti	Ta	Co	Cr	Mo	W	Re
Al	191.608	-1.045	-0.588	-31.595	-61.961	-0.834	-2.323	-1.703
Ti	-1.045	4.517	0.000	-0.835	-2.560	-0.010	-0.100	-0.004
Ta	-0.588	0.000	0.058	-0.012	-0.954	0.006	-0.039	0.027
Co	-31.595	-0.835	-0.115	136.521	-82.954	-0.445	-3.222	-0.431
Cr	-61.961	-2.560	-0.954	-82.954	307.745	-1.739	-7.564	-2.896
Mo	-0.834	-0.010	0.006	-0.445	-1.739	2.057	-0.069	0.015
W	-2.323	-0.100	-0.039	-3.222	-7.564	-0.069	19.453	-0.118
Re	-1.703	-0.004	0.027	-0.431	-2.896	0.015	-0.118	0.892

Declaration of Competing Interest

The authors declare that they have no known competing financial interests or personal relationships that could have appeared to influence the work reported in this paper.

Acknowledgements

The authors would like to acknowledge the supports provided by the National Science and Technology Major Project (Grant No.: 2017-VI-0002-0072), National Natural Science Foundation of China (Grant No.: 51631008 and 91860201) and Key-Area Research and Development Program of Guangdong Province (Grant No.:2019B010943001) and 111 Project (Grant No.: B170003). S.A. would like to acknowledge financial support from the Alexander von Humboldt Foundation.

References

[1] R.C. Reed, The Superalloys: Fundamentals and Applications, Cambridge University Press, 2006.
[2] T.M. Pollock, S. Tin, Nickel-based superalloys for advanced turbine engines: chemistry, microstructure and properties, J. Propul. Power. 22 (2006) 361–374.
[3] O.M. Horst, D. Adler, P. Git, H. Wang, G. Eggeler, Exploring the fundamentals of Ni-based Superalloy single crystal (SX) alloy design: Chemical composition vs. microstructure, Mater. Des. 195 (2020) 108976.
[4] R. Hashizume, A. Yoshinari, T. Kiyono, Y. Murata, M. Morinaga, Development of Ni based single crystal superalloys for power generation gas turbine blades, Energy Mater 2 (2009) 5–12.
[5] M.V. Acharya, G.E. Fuchs, The effect of long-term thermal exposures on the microstructure and properties of CMSX-10 single crystal Ni-base superalloys, Mater. Sci. Eng., A. 381 (2004) 143–153.
[6] Z.X. Shi, J.R. Li, S.Z. Liu, Effect of long term aging on microstructure and stress rupture properties of a nickel based single crystal superalloy, Prog. Nat. Sci.: Mater. Int. 22 (2012) 426–432.
[7] J. Tiley, G.B. Viswanathan, R. Srinivasan, R. Banerjee, D.M. Dimiduk, H.L. Fraser, Coarsening kinetics of γ' precipitates in the commercial nickel base superalloy René 88 DT, Acta Mater 57 (2009) 2538–2549.
[8] D. Mclean, Predicting growth of γ' in nickel alloys, Met. Sci. 18 (1984) 249–256.
[9] J.X. Zhang, J.C. Wang, H. Harada, Y. Koizumi, The effect of lattice misfit on the dislocation motion in superalloys during high-temperature low-stress creep, Acta Mater 53 (2005) 4623–4633.
[10] L.J. Carroll, Q. Feng, T.M. Pollock, Interfacial dislocation networks and creep in directional coarsened Ru-containing Nickel-base single-crystal superalloys, Metall. Mater. Trans. A. 39 (2008) 1290–1307.
[11] F. Lu, L.F. Li, S. Antonov, Y.F. Zheng, H.L. Fraser, D. Wang, J. Zhang, Q. Feng, Effect of Re on long-term creep behavior of Nickel-based single-crystal superalloys for industrial gas turbine applications, in Superalloys 2020, 2020, pp. 218-227.
[12] M. Fährmann, P. Fratzl, O. Paris, E. Fährmann, W.C. Johnson, Influence of coherency stress on microstructural evolution in model Ni-Al-Mo alloys, Acta Metall. Mater. 43 (1995) 1007–1022.
[13] I.M. Lifshitz, V.V. Slyozov, The kinetics of precipitation from supersaturated solid solutions, J. Phys. Chem. Solids. 19 (1961) 35–50.
[14] C. Wagner, Theorie der Alterung von Niederschlägen durch Umlösen, Zeitschrift für Elektrochemie, Berichte der Bunsengesellschaft für physikalische Chemie 65 (2015) 581–591.
[15] A.J. Ardell, The effect of volume fraction on particle coarsening: theoretical considerations, Acta Metall 20 (1972) 61–71.
[16] C.K.L. Davies, P. Nash, R.N. Stevens, Precipitation in Ni-Co-Al alloys, J. Mater. Sci. 15 (1980) 1521–1532.
[17] A.D. Brailsford, P. Wynblatt, The dependence of Ostwald ripening kinetics on particle volume fraction, Acta Metall 27 (1979) 489–497.
[18] C.J. Kuehmann, P.W. Voorhees, Ostwald ripening in ternary alloys, Metall. Mater. Trans. A. 27 (1996) 937–943.
[19] T. Philippe, P.W. Voorhees, Ostwald ripening in multicomponent alloys, Acta Mater 61 (2013) 4237–4244.
[20] A.J. Ardell, Gradient energy, interfacial energy and interface width, Scr. Mater. 66 (2012) 423–426.
[21] A.J. Ardell, Trans-interface-diffusion-controlled coarsening of γ' precipitates in ternary Ni–Al–Cr alloys, Acta Mater 61 (2013) 7828–7840.
[22] A.J. Ardell, V. Ozolins, Trans-interface diffusion-controlled coarsening, Nat. Mater. 4 (2005) 309–316.
[23] W. Sun, Kinetics for coarsening co-controlled by diffusion and a reversible interface reaction, Acta Mater 55 (2007) 313–320.
[24] J.C Zhang, L. Liu, T.W. Huang, J. Chen, K.L. Cao, X.X. Liu, J. Zhang, H.Z. Fu, Coarsening kinetics of γ' precipitates in a Re-containing Ni-based single crystal superalloy during long-term aging, J. Mater. Sci. Technol. 62 (2021) 1–10.
[25] J.X. Chang, D. Wang, X.G. Liu, L.H. Lou, J. Zhang, Effect of rhenium addition on hot corrosion resistance of Ni-based single crystal superalloys, Metall. Mater. Trans. A. 49 (2018) 1–10.
[26] R.C. Reed, J.J. Moverare, A. Sato, F. Karlsson, M. Hasselqvist, A new single crystal superalloy for power generation applications, Superalloys 2012 (2012) 197–204.
[27] S. Antonov, M. Detrois, D. Isheim, D.N. Seidman, R.C. Helmink, R.L. Goetz, E. Sun, S. Tin, Comparison of thermodynamic database models and APT data for strength modeling in high Nb content γ–γ' Ni-base superalloys, Mater. Des. 86 (2015) 649–655.
[28] E.A. Lass, D.J. Sauza, D.C. Dunand, D.N. Seidman, Multicomponent γ'-strengthened Co-based superalloys with increased solvus temperatures and reduced mass densities, Acta Mater 147 (2018) 284–295.
[29] E.Y. Plotnikov, Z. Mao, R.D. Noebe, D.N. Seidman, Temporal evolution of the γ(fcc)/γ'($L1_2$) interfacial width in binary Ni–Al alloys, Scr. Mater. 70 (2014) 51–54.
[30] C.K. Sudbrack, K.E. Yoon, R.D. Noebe, D.N. Seidman, Temporal evolution of the nanostructure and phase compositions in a model Ni-Al-Cr alloy, Acta Mater 54 (2006) 3199–3210.
[31] P.J. MacSleyne, P.J. Simmons, M. De Graef, On the use of 2-D moment invariants for the automated classification of particle shapes, Acta Mater 56 (2008) 427–437.
[32] H.A. Kuhn, H. Biermann, T. Ungar, H. Mughrabi, An X-ray study of creep--deformation induced changes of the lattice mismatch in the γ'-hardened monocrystalline nickel-base superalloy SRR 99, Acta Metall. Mater. 39 (1991) 2783–2794.
[33] C.H. Zenk, I. Povstugar, R. Li, F. Rinaldi, S. Neumeier, D. Raabe, M. Göken, A novel type of Co-Ti-Cr-base γ/γ' superalloys with low mass density, Acta Mater 135 (2017) 244–251.
[34] K. Thompson, D. Lawrence, D.J. Larson, J.D. Olson, T.F. Kelly, B. Gorman, In situ site-specific specimen preparation for atom probe tomography, Ultramicroscopy 107 (2007) 131–139.
[35] M. Doi, T. Miyazaki, T. Wakatsuki, The effect of elastic interaction energy on the morphology of γ' precipitates in nickel-based alloys, Mater. Sci. Eng. 67 (1984) 247–253.
[36] S. Antonov, E. Sun, S. Tin, Synchrotron in-situ aging study and correlations to the γ' phase instabilities in a high-refractory content γ-γ' Ni-base superalloy, Metall. Mater. Trans. A. 49 (2018) 3885–3895.
[37] E.Y. Plotnikov, Z. Mao, S.I. Baik, M. Yildirim, D.N. Seidman, A correlative four-dimensional study of phase separation at the subnanoscale to nanoscale of a NiAl Alloy, Acta Mater 171 (2019) 306–333.

[38] R. Mitchell, M. Preuss, M. Hardy, S. Tin, Influence of composition and cooling rate on constrained and unconstrained lattice parameters in advanced polycrystalline nickel–base superalloys, Mater. Sci. Eng., A. 423 (2006) 282–291.
[39] O.C. Hellman, J.A. Vandenbroucke, J. Rüsing, D. Isheim, D.N. Seidman, Analysis of three-dimensional atom-probe data by the proximity histogram, Microsc. Microanal. 6 (2000) 437–444.
[40] Y. Amouyal, Z. Mao, C. Booth-Morrison, D.N. Seidman, On the interplay between tungsten and tantalum atoms in Ni-based superalloys: An atom-probe tomographic and first-principles study, Appl. Phys. Lett. 94 (2009) 041917.
[41] L. Xu, C.G. Tian, C.Y. Cui, Y.F. Gu, X. Sun, Morphology evolution of unstable γ' in Ni-Co based superalloy, Mater. Sci. Technol. 30 (2014) 962–967.
[42] X. Zhao, R. Duddu, S.P.A. Bordas, J. Qu, Effects of elastic strain energy and interfacial stress on the equilibrium morphology of misfit particles in heterogeneous solids, J. Mech. Phys. Solids 61 (2013) 1433–1445.
[43] R. Watanabe, T. Kuno, Alloy design of nickel-base precipitation hardened superalloys, Trans. Iron Steel Inst. Jpn. 16 (1976) 437–446.
[44] Y. Huang, Z. Mao, R.D. Noebe, D.N. Seidmen, Effects of tungsten and rhenium additions on phase-separation in a model Ni-Al-Cr-W-Re superalloy: A four-dimensional study, J. Alloys Compd. 799 (2019) 377–388.
[45] D.J. Sauza, D.C. Dunand, R.D. Noebe, D.N. Seidman, γ'-($L1_2$) precipitate evolution during isothermal aging of a Co-Al-W-Ni superalloy, Acta Mater 164 (2019) 654–662.
[46] Y. Amouyal, D.N. Seidman, An atom-probe tomographic study of freckle formation in a nickel-based superalloy, Acta Mater 59 (2011) 6729–6742.
[47] X. Li, N. Saunders, A.P. Miodownik, The coarsening kinetics of γ' particles in nickel-based alloys, Metall. Mater. Trans. A. 33 (2002) 3367–3373.
[48] A. Baldan, Review progress in Ostwald ripening theories and their applications to nickel-base superalloys Part I: Ostwald ripening theories, J. Mater. Sci. 37 (2002) 2171–2202.
[49] J.W. Cahn, J.E. Hilliard, Free energy of a nonuniform system. I. Interfacial free energy, J. Chem. Phys. 28 (1958) 258–267.
[50] B. Sundman, B. Jansson, J.O. Andersson, The Thermo-Calc databank system, Calphad 9 (1985) 153–190.
[51] A.F. Giamei, D.L. Anton, Rhenium additions to a Ni-base superalloy: Effects on microstructure, Metall. Trans. A. 16 (1985) 1997–2005.
[52] W.Z. Wang, T. Jin, J.L. Liu, X.F. Sun, H.R. Guan, Z.Q. Hu, Role of Re and Co on microstructures and γ' coarsening in single crystal superalloys, Mater. Sci. Eng., A. 479 (2008) 148–156.
[53] H.A. Calderon, P.W. Voorhees, J.L. Murray, G. Kostorz, Ostwald ripening in concentrated alloys, Acta Metall. Mater. 42 (1994) 991–1000.
[54] Z. Zhu, H. Basoalto, N. Warnken, R.C. Reed, A model for the creep deformation behaviour of nickel-based single crystal superalloys, Acta Mater 60 (2012) 4888–4900.
[55] Z.X. Shi, S.Z. Liu, X.G. Wang, J.R. Li, Effects of Cr content on microstructure and mechanical properties of single crystal superalloy, Trans. Nonferrous Met. Soc. China. 25 (2015) 776–782.
[56] D.S. Ng, D-W. Chung, J.P. Toinin, D.N. Seidman, D.C. Dunand, E.A. Lass, Effect of Cr additions on a γ-γ' microstructure and creep behavior of a Co-based superalloy with low W content, Mater. Sci. Eng., A. 778 (2020) 139108.
[57] X.L. Zhuang, S. Antonov, L.F. Li, Q. Feng, Effect of alloying elements on the coarsening rate of γ' precipitates in multi-component CoNi-based superalloys with high Cr content, Scr. Mater. 202 (2021) 114004.
[58] S. Meher, M. Carroll, T. Pollock, L. Carroll, Designing nickel base alloys for microstructural stability through low γ-γ' interfacial energy and lattice misfit, Mater. Des. 140 (2018) 249–256.
[59] A. Heckl, S. Neumeier, M. Göken, R.F. Singer, The effect of Re and Ru on γ/γ' microstructure, γ-solid solution strengthening and creep strength in nickel-base superalloys, Mater. Sci. Eng., A. 528 (2011) 3435–3444.
[60] E. Fleischmann, M.K. Miller, E. Affeldt, U. Glatzel, Quantitative experimental determination of the solid solution hardening potential of rhenium, tungsten and molybdenum in single-crystal nickel-based superalloys, Acta Mater 87 (2015) 350–356.
[61] C. Booth-Morrison, R.D. Noebe, D.N. Seidman, Effects of tantalum on the temporal evolution of a model Ni–Al–Cr superalloy during phase decomposition, Acta Mater 57 (2009) 909–920.
[62] A.J. Ardell, Quantitative predictions of the trans-interface diffusion-controlled theory of particle coarsening, Acta Mater 58 (2010) 4325–4331.
[63] A. Baldan, Review progress in Ostwald ripening theories and their applications to the γ'-precipitates in nickel-base superalloys Part II Nickel-base superalloys, J. Mater. Sci. 37 (2002) 2379–2405.
[64] A.J. Ardell, An application of the theory of particle coarsening: The γ' precipitate in Ni-Al alloys, Acta Metall 16 (1968) 511–516.
[65] M.M.P. Janssen, Diffusion in the nickel-rich part of the Ni−Al system at 1000°C to 1300°C; Ni_3Al layer growth, diffusion coefficients, and interface concentrations, Metall. Trans. 4 (1973) 1623–1633.
[66] T. Ikeda, A. Almazouzi, H. Numakura, M. Koiwa, W. Sprengel, H. Nakajima, Single-phase interdiffusion in Ni_3Al, Acta Mater 46 (1998) 5369–5376.
[67] K.E. Yoon, R.D. Noebe, D.N. Seidman, Effects of rhenium addition on the temporal evolution of the nanostructure and chemistry of a model Ni–Cr–Al superalloy. I: Experimental observations, Acta Mater 55 (2007) 1145–1157.
[68] J. Lapin, M. Gebura, T. Pelachová, M. Nazmy, Coarsening kinetics of cuboidal γ' precipitates in single crystal nickel base superalloy CMSX-4, Kovove Mater 46 (2008) 313–322.
[69] P. Pandey, A. Sawant, N. Baler, S.K. Makineni, K. Chattopadhyay, Effect of Ru addition on γ/γ' microstructural stability in a low-density CoNi based superalloy, Scr. Mater. 208 (2022) 114318.
[70] P. Pandey, A. Sawant, B. Nithin, Z. Peng, S.K. Makineni, B. Gault, K. Chattopadhyay, On the effect of Re addition on microstructural evolution of a CoNi-based superalloy, Acta Mater 168 (2019) 37–51.